Nitriding aluminum alloys by N-multicharged ions implantation: Correlation between surface strengthening and microstructure modifications

E. Hug [a,*], S. Thibault [b], D. Chateigner [a,c], L. Maunoury [d]

[a] Laboratoire de Cristallographie et Sciences des Matériaux, ENSICAEN, Université de Caen Basse-Normandie, CNRS, 6 bd. Maréchal Juin, 14050 Caen, France
[b] ENSICAEN, 6 bd. Maréchal Juin, 14050 Caen, France
[c] IUT-Caen, Université de Caen Basse-Normandie, 6 bd. Maréchal Juin, 14050 Caen, France
[d] Grand Accélérateur National d'Ions Lourds (GANIL), bd. Henri Becquerel, 14076 Caen Cedex 05, France

ARTICLE INFO

ABSTRACT

This paper deals with the surface strengthening of aluminum alloys by means of a new process allowing multi-charged nitrogen ion implantation. X-ray photoelectron spectroscopy, grazing-incidence X-ray diffraction and atomic force microscopy were used to study microstructural changes involved by implantation. This microstructural study revealed the formation of AlN and AlONγ due to the low nitrogen concentration gradient obtained with multi-charged implantation. Nanoindentation and wear tests were performed to evaluate the mechanical properties of implanted surfaces. A significant improvement of wear resistance was observed as a consequence of the nitride protective layer formation. The observed surface hardening is attributed to both AlONγ and AlN formations and to the precipitation-induced stress.

© 2012 Elsevier B.V. All rights reserved.

1. Introduction

Aluminum alloys are well known for their low weight and good mechanical properties. They are used in many industrial applications, such as automotive and aeronautics. However, in some severe conditions, they can exhibit a lack of wear resistance and consequently their surfaces have to be treated to increase superficial hardness and extend their life time.

Strain and precipitation-hardened Al-base alloys are very sensitive to temperature conditions. Strain hardening occurs from recrystallization processes, and precipitates coalesce, both usually at low temperatures in such alloys. Consequently, thermochemical surface treatments commonly used for steels, which involve an increase of temperature for long periods of time, cannot be applied to these materials. As a result, anodization is the most common surface treatment used to improve surface wear resistance in aluminum industry. However, despite the very good results that they provide, anodization techniques are very pollutant and greener physico-chemical processes would be advantageous substitutes.

Alternative surface treatments such as physical vapor deposition (PVD) or in general plasma based technologies successfully achieved in the last decades an increase in life time products with a minimized environment impact. Among them, ion implantation can be used to enhance aluminum wear resistance performing immersed ion implantation [1–4] or direct implantation, which the study presented in this paper concerns. Many investigations have been performed on mono or multi-energetic nitrogen (successive implantations with decreasing energies) implantation into aluminum. A lot of contributions focus on microstructural modifications occurring during implantation [5–11]. Others are concerned by functional properties of N-implanted materials [12,13] reporting the formation of a hard nitride layer which protects the substrate from wear [14] and corrosion [15].

In this study, we propose to correlate the evolution of microstructure to the surface strengthening of both commercial pure aluminum (Al-1050) and aluminum alloys (Al-2024) impinged by means of multi-charged nitrogen ions in order to identify the mechanisms involved. To this end an implantation process based on multi-charged ion implantation was used [16], made possible thanks to the use of compact electron cyclotron resonance (ECR) ion source as particle supplier and accelerator [17]. The obtained results are also used to compare traditional single/multi-energetic N-implantations with multi-charged implantations. Microstructural analysis is firstly presented and confronted with results obtained by hardness and wear tests. Then, we discuss the different phenomena responsible for the surface properties modifications induced by the implantation. Most of the results shown in this study concern Al-1050 but complementary experiments performed on Al-2024 help the comparison between strain (Al-1050) and structural (Al-2024) hardening behaviors.

* Corresponding author at: Laboratoire CRISMAT, Ensicaen, Université de Caen, CNRS, 6 Bd Maréchal Juin, 14050 Caen, France. Tel.: +33 2 31 45 13 13; fax: +33 2 31 95 16 00.
E-mail address: eric.hug@ensicaen.fr (E. Hug).

2. Experimental procedure

2.1. Samples preparation

Two aluminum alloys were studied in this work: commercially pure Al-1050, used essentially for packaging applications, and to less extent Al-2024, one of the most used alloys in industry because of its larger mechanical properties due to precipitation hardening. Al-1050 sheets contained 99.5% in weight of aluminum and were annealed at 673 K for 10 h in order to remove strain-hardening coming from cold-rolling, and to obtain a recrystallized structure. A 20 μm average grain size was measured by light microscopy image analysis and confirmed by EBSD. Al-2024 rods were used as received. Samples (thickness: 10 mm, diameter: 30 mm) were mechanically ground with SiC paper and polished to a mirror grade with diamond paste. Electrochemical polishing was performed on samples for nanoindentation and X-ray diffraction measurements. A mix of 2-butoxyethanol and perchloric acid (60%) as electrolyte was used, and a 20 V bias voltage applied between sample and cathode for 20 s. A pure AlN sample (thickness: 0.25 mm, length: 10 mm, width: 10 mm) was treated as received to obtain aluminum nitride intrinsic properties (hardness and wear tests).

2.2. Implantation procedure

Nitrogen implantation was performed using a micro-implanter described elsewhere [18]. The set-up is based on a compact multi-charged ion source and a small vacuum chamber. The ion source is an ECR type named Microgan from Pantechnik. It is 30 cm in height, 15 cm in diameter and weighs 11 kg. It operates at a frequency of 10 GHz. It is able to provide beams of multicharged ions in several mA ranges and charge states up to $4+$ in the case of nitrogen ions. The average charge is around $1.4+$. The beam is extracted and accelerated under a bias voltage of 40 kV. The resulting average implantation energy due to multiple accelerations was around 60 keV. Using multi-charged N-ions makes the creation of a low concentration gradient along the sample thickness possible. The projected range R_p of ion implantation was calculated with the help of the S.R.I.M. software [15] giving a value of about 120 nm. The maximum depth reached by nitrogen ions is approximately 400 nm. Implantation durations ranged between 10 and 60 s/cm², which corresponds to ion fluencies in the range of $5 \cdot 10^{17}$–$3 \cdot 10^{18}$ ions/cm². These values do not consider saturation effects shown by Miyagawa et al. [19]. As a consequence, indicated fluencies are implanted ones but not retained ones. Using the previous fluence and voltage ranges, typical thermal loads between 0.2 and 2.5 kW/cm² are expected. In order to avoid the harmful effects of this heating, a cooling system is integrated inside the sample holder. Temperature measurements on samples were made during implantation to ensure they did not exceed 373 K. The pressure in the vacuum chamber during the implantation stage was maintained at approximately 10^{-6} mbar in order to avoid oxygen contamination and to maintain a good ion transport to the target.

2.3. Microstructural investigations

Microstructural studies were performed in details on Al-1050 samples. Chemical composition and ion species identification were obtained with XPS analysis using a VG Escalab 220XL instrument working with energy value of 1486.6 eV. A 4 keV argon-ion beam allowed us to obtain concentration depth profiles.

Grazing incidence XRD (GIXRD) patterns of implanted and pristine samples were measured on a four-circle INEL diffractometer equipped with a curved position sensitive detector (CPS120) able to span at once the whole 2θ range of interest. We used the CuKα radiation and treated the data using the Material Analysis Using Diffraction (MAUD) software [20]. The incidence angle was set to 1° in order to obtain data principally from the implanted volume. These results were obtained by Rietveld refinement [21] using MAUD software [22]. The isotropic mean crystallite size of AlNα (mean coherently scattering domains considered as spheres) was refined from direct Fourier analysis [23] on the whole-powder pattern. Instrumental broadening was determined using the NIST LaB₆ 660srm standard powder and deconvolved from the experimentally measured diagram. We used the AlNα structure as available on the Crystallography Open Database [24].

Surface topography was studied by atomic force microscopy using a NanoScope device in tapping mode with a Si₃N₄ tip. A 600×600 nm area was scanned for each sample.

2.4. Mechanical properties testing

Superficial hardness profiles were obtained with a MTS XP nanoindentation device using the continuous stiffness measurement mode.
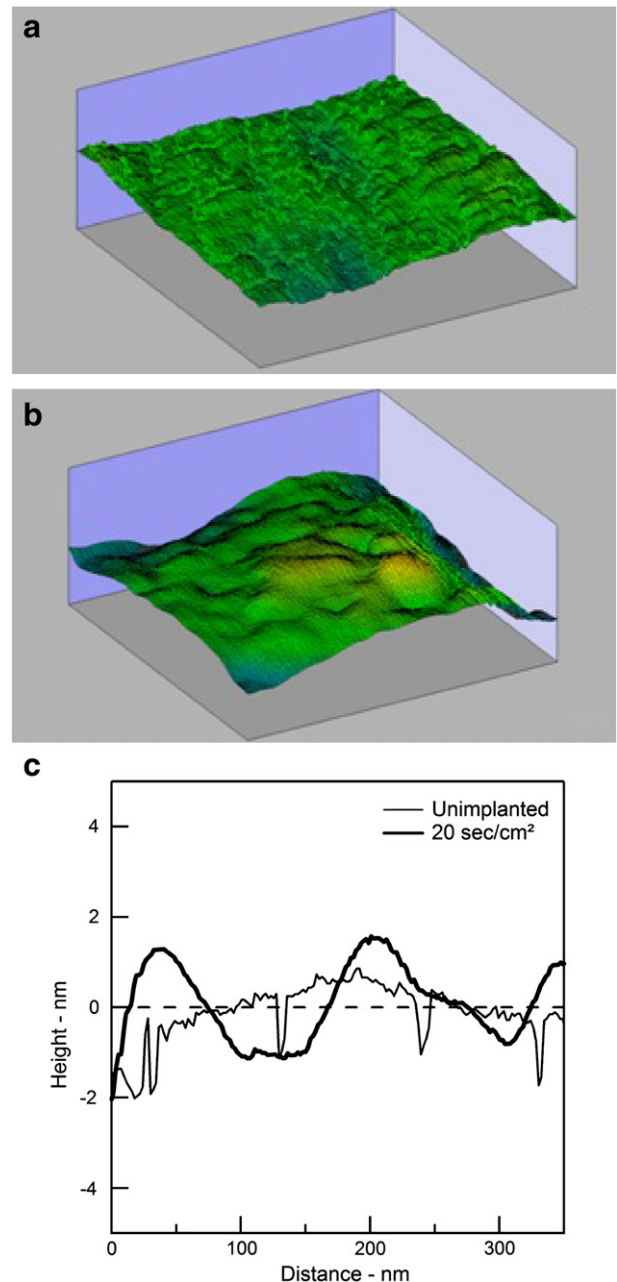

Fig. 1. AFM surface topography (600 nm × 600 nm) of (a) unimplanted and (b) 20 s/cm² implanted samples. Evolution of the surface mean line for both samples (c).

On each sample, two matrixes of indents were performed with a Berkovich tip (25 indents − 5×5-; X–Y-space: 100 μm; indentation depth: 2 μm). Tribological tests were performed with a CSM tribometer, using a 6 mm diameter 100C6 ball. A 0.25 N load was applied. The rotation speed was fixed to 0.1 mm/s. Residual tracks profiles were determined with profilometry measurements.

3. Results and discussion

3.1. Microstructure modifications

AFM analysis revealed an expected sputtering of the surface resulting from a smoothing phenomenon. Fig. 1(a) and (b) shows the surface topography before and after implantation. Acute angles due to polishing tracks totally disappear after implantation, indicating a decrease in the surface roughness. However, the implantation process develops an undulation of the surface mean line, as we can see in Fig. 1(c). Both topography changes are attributed to the surface sputtering occurring during implantation.

Atomic concentration profiles of aluminum, nitrogen, carbon and oxygen obtained by XPS analysis of the 40 s/cm² implanted sample are plotted in Fig. 2. As expected, the implantation of multicharged ions forms a low gradient of nitrogen concentration directed to the large depths (corresponding to the higher sputtering times). The nitrogen concentration profile is quite similar to the one obtained by Leblond et al. [25] using successive multi-energetic implantations (40 keV, 25 keV and 10 keV). A comparison with virgin sample spectra confirms the inexistence of carbon or oxygen pollution due to the implantation process. The high oxygen concentration measured near the surface region is the result of natural passivation of aluminum surface leading to the formation of aluminum hydroxide $Al(OH)_3$. Maximum nitrogen atomic concentration is obtained after 90 min of sputtering for all studied samples and is respectively 0, 34, 35 and 40% for pristine, 10 s/cm², 30 s/cm² and 40 s/cm² for implanted samples.

The analysis of chemical shifts on elemental spectra provides interesting results concerning the chemical species contained in the samples. The Al(2p) spectrum of the virgin sample (Fig. 3(a)) clearly exhibits two peaks located at 76.6 eV and 73.2 eV corresponding to Al−O (surface region) and metallic Al (core region) bonds, respectively. After a 10 s/cm² implantation (Fig. 3(b)), a third peak appears at an intermediate depth with an energy level of 74.5 eV. According to the nitrogen atomic concentration obtained and to other works [9,25–28] dealing with nitrogen implanted unalloyed aluminum, this peak
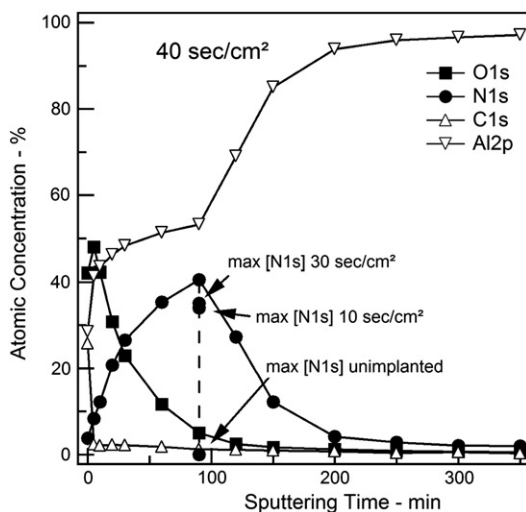

Fig. 2. Concentration profiles of Al, N, O and C for the 40 s/cm² implanted sample. Maxima of nitrogen concentrations are also plotted for unimplanted, 10 s/cm² and 30 s/cm² implanted samples (XPS analysis).
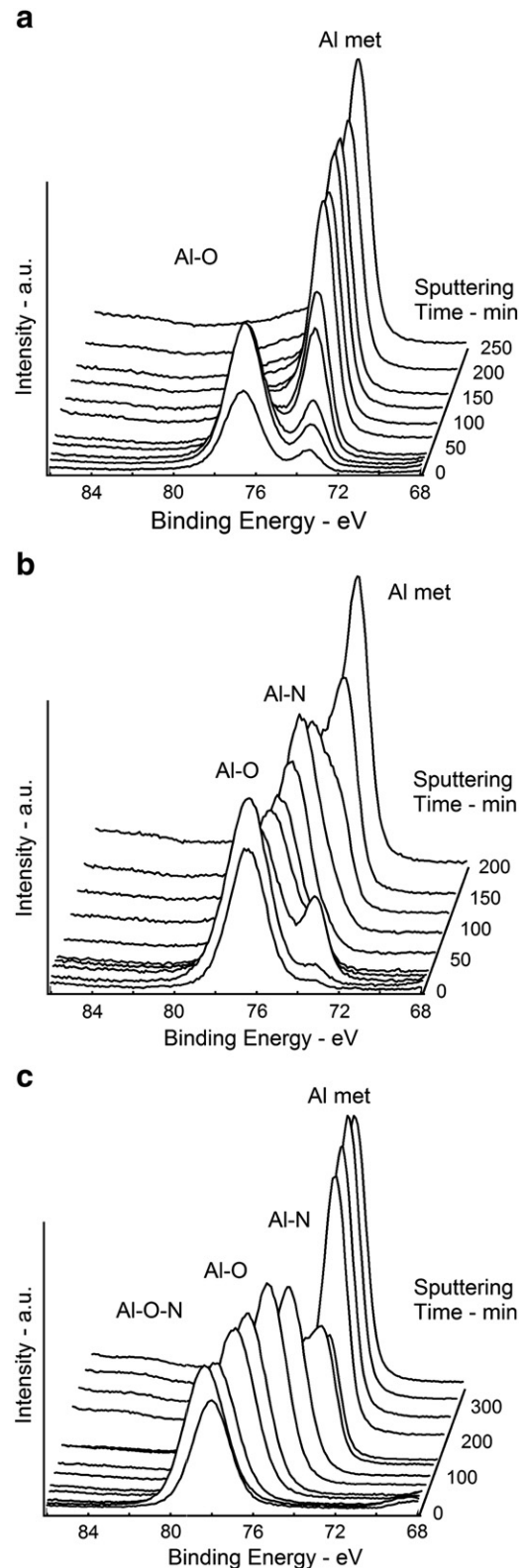

Fig. 3. Al(2p) spectra for (a) unimplanted, (b) 10 s/cm² implanted and (c) 40 s/cm² implanted samples.

might be associated with Al−N bonds. Another peak appears after 40 s/cm² at an energy of 78.4 eV for the shorter sputtering times (Fig. 3(c)).

Fig. 4 shows O(1s) and N(1s) spectra obtained after 5 min of sputtering on the virgin sample and on 10 s/cm² and 40 s/cm² implanted

samples. The chemical shift of O(1s) peak, from 533.3 eV to 534.5 eV indicates that the oxygen bonds are modified under irradiation at 10 s/cm^2 and 40 s/cm^2 and are no longer simple Al–O ones. The N(1s) spectrum exhibits two peaks (around 400 eV and 407 eV) for the 40 s/cm^2 implanted sample whereas only one (around 400 eV) is visible for the 10 s/cm^2 implanted sample, this latter corresponding to N–Al bonds. These results demonstrate that nitrogen is present in the near surface of our implanted samples, with two kinds of bonds. The larger binding energy of the second peak indicates that nitrogen is more oxidized for this bond. This observation could be associated to the existence of the previously observed peak located at 78.4 eV in the Al(2p) spectrum of the 40 s/cm^2 implanted sample, which could therefore be linked to the formation of Al–O–N bonds. Such chemical shift of N(1s) peak have already been observed by Figueroa et al. [29] for N-implanted Al and have been attributed to N–O bond.

A comparison between the atomic concentrations measured on the surface region of the 40 s/cm^2 implanted sample and previous experiments performed by EDS on AlONγ by McCauley et al. [30] is presented in Table 1. It confirms the existence of AlONγ after nitrogen implantation. The interpenetration of nitride and oxide layers, allowed by the low nitrogen gradient, has led to the formation of this intermediary compound. The examination of oxygen concentration profiles does not show any progressive oxygen content toward the core region
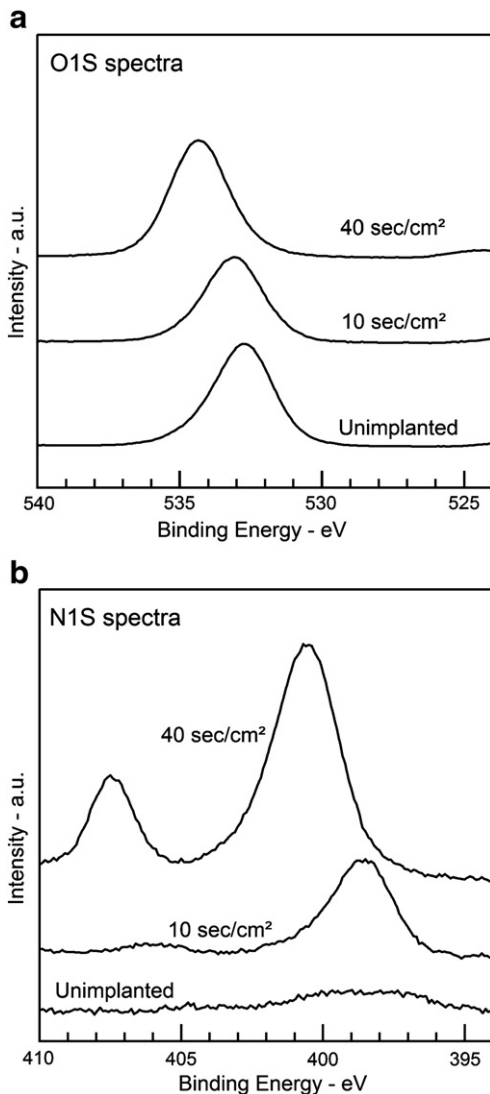
Table 1

Comparison of elements concentrations measured by XPS on an implanted Al-1050 sample (near the surface region) and elements concentrations measured by EDS on sintered AlONγ by McCauley et al. [30].

Element	XPS measurement Present study	EDS measurement of AlONγ [30]
Al	42%	41%
O	49%	51%
N	9%	8%

during implantation. We can also assume that the oxynitride phase is formed in the first 10 nm of thickness, where the oxide layer is initially present.

Using grazing incidence X-rays at a 1° incidence angle, XRD scans allows the crystallographic characterization of the implanted surface. Under these asymmetric conditions, Eq. (1) gives the general expression for the depth x from which the observed diffracted intensity comes.

$$x = -\frac{1}{\mu_{RX}M}\ln\left(1-\frac{I}{I_0}\right) \tag{1}$$

I_0 is the incident intensity, μ_{RX} is the linear absorption coefficient of aluminum for the used radiation ($\mu_{XR} = 12{,}966\ \text{m}^{-1}$) and M is a geometric factor which depends on the angles used for the measurements [23].

In our experimental settings, around 23% of the incident intensity is diffracted in the implanted depth (~400 nm). This is confirmed by the diffraction spectra (Fig. 5) of the 40 s/cm^2 implanted samples, clearly displaying broad peaks corresponding to the existence of hexagonal close-packed aluminum nitride AlNα [31]. All spectra of implanted samples reveal these peaks in which expected positions are reported in Table 2. However, it was impossible to detect the presence of AlONγ with GIXRD. If we assume that AlONγ is only present in the first 10 nm of thickness, the ratio I/I_0 coming from this area falls to a value of 0.6%.

The broadening of AlN diffraction peaks is due to the small size of the crystallites, coherent scattering domains of this phase. The study of others samples implanted with different fluencies allowed us to affirm that the size of AlN crystallites tends to be larger for higher fluences and falls between the range of 4 and 7 nm (Table 3). These results are in good agreement with previous studies [6,12,27,28,32,33].

Despite of the broadening of the Al diffraction peaks, due to the combined effect of aluminum grain size (d = 20 μm) and grazing incidence diffraction [23], the relative evolution of the aluminum lattice parameter a_{Al} during implantation can be estimated (Table 3) from whole-pattern fitting analysis. Details of this technique can be found in a recent article concerning Ba(Sr, Ti)O$_3$ thin films [34]. The obtained results qualitatively illustrate the evolution of the residual strain state of the matrix. A first step of expansion of the matrix is highlighted followed by a relaxation and the apparition of a compressive state. At 40 s/cm^2, a second relaxation seems to be initiated.

The expansion step is attributed to the formation of metastable interstitial solid solution of N into Al (Al-octahedral site radius = 5 nm, N-atomic radius = 9.2 nm) forming the often called AlNβ in a fcc space group [2,35–37]. This solution is obtained thanks to a hyperquenching phenomenon frequently observed on irradiated materials. The proximity of AlNβ and Al diffraction peaks (Table 2) made it impossible for a clear identification on the diffraction spectra. As N-fluence increases, internal stresses get higher and lead to crystallographic shearing on the {111} slipping planes as usual for fcc structures. A crystallographic rearrangement of the substrate takes place, changing from an ABCABC… to ABAB… stack, corresponding to Al (fcc) → AlNα (hcp) transformation [6]. The consequence of this latter is a reduction in internal energy and thus a matrix relaxation. This transformation leads to the existence
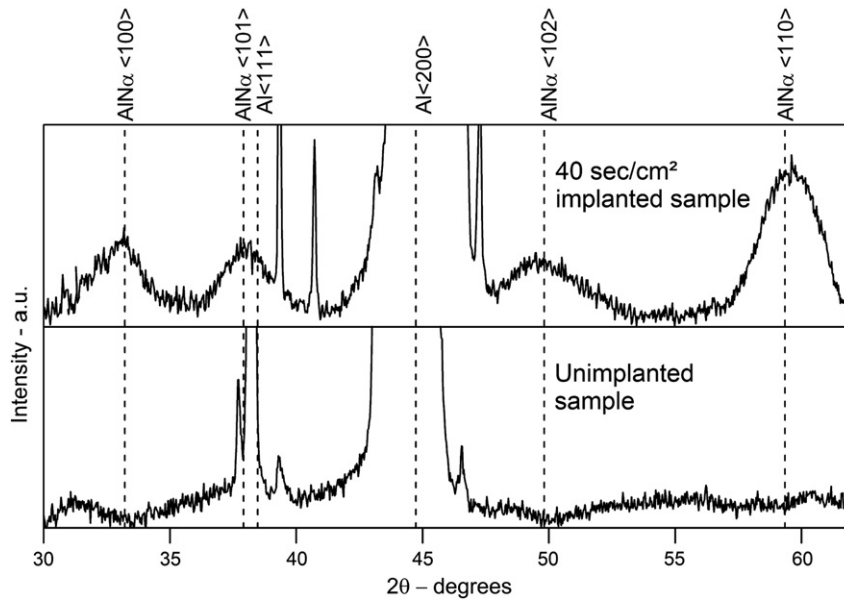

Fig. 4. (a) O(1s) and (b) N(1s) spectra of unimplanted, 10 s/cm^2 implanted and 40 s/cm^2 implanted samples near the surface region (sputtered time of 5 min).

Fig. 5. GIXRD spectra of (down) unimplanted and (up) 40 s/cm² implanted Al-1050 sample showing the existence of AlNα.

of epitaxial relationships imposed by the habitat plane Al{111} of the transformation. The well-known Al{111}//AlNα{002} [6,27,28] epitaxial relationship makes the observed growth of AlN coherent, which implies the apparition of compressive stresses. The very low intensity of an Al{111} diffraction peak ($I_{Al\{111\}}/I_{Al\{200\}} = 1/10$, instead of 100/47 for theoretical isotropic aluminum) reveals an initial crystallographic texture which could explain the absence of AlNα{002} diffraction peak. This initial texture is closely related to the laminated state of the pristine samples. The start of a second relaxation step could be explained by the beginning of incoherent growth.

3.2. Hardness and wear properties

Fig. 6 shows typical hardness profiles measured on unimplanted and implanted 1050 samples. The shape of the profile is close to the nitrogen concentration profile shown in Fig. 1. The hardness peak is located between 20 nm and 40 nm from the surface edge. The 1/3 ratio between the hardness peak and the nitrogen concentration peak positions (120 nm) have already been observed [6,25,27,28,38,39]. This phenomenon is due to the strained area, which exceeds the indentation depth. Even though the indentation depth is ranged in the nitride

region, the aluminum bulk, which is softer, is also stressed and contributes to the mechanical response of the sample.

Average hardness peak values increase with the implanted fluence until 30 s/cm², where the material exhibits an average hardness peak value of 11 GPa (Fig. 7). It corresponds to a hardness increase of around thirty times, as shown in previous results reported by Leblond et al. [25] using successive multi-energetic implantations. This value is very close to the AlN hardness evaluated to 12 GPa on our reference sample. Prolonging implantation induces a decrease in the average hardness peak.

Tribological tests were performed in order to observe the effect of implantation on wear resistance. Fig. 8 shows the evolution of the friction coefficient μ during the test. For the virgin sample, μ = 1 for the whole duration of the test. 10 s/cm² and 30 s/cm² implanted samples have quite the same friction behavior and are not presented here. A 40 s/cm² implantation is necessary to modify the friction properties of the aluminum surface. At the beginning of the test, the friction coefficient of this latter sample is close to that of AlN (μ = 0.2) and increases until the layer fracture occurring after 220 laps.

Table 2
Lattice parameters of Al, AlNα and AlNβ, and main diffraction peak positions.

Phase	a in nm	c in nm	2θ positions of most important diffraction peaks with λ = 0.1542 nm (Cu Kα) in degree		
Al (fcc)	0.405	–	38.47 <111>	44.73 <200>	65.13 <220>
AlNα (hcp)	0.311	0.498	33.21 <100>	36.04 <002>	37.91 <101>
AlNβ (fcc)	0.412	–	37.78 <111>	43.91 <200>	63.83 <220>

Table 3
Relative variation of the Al lattice parameter and mean isotropic sizes of AlN crystallites for various implanted fluences.

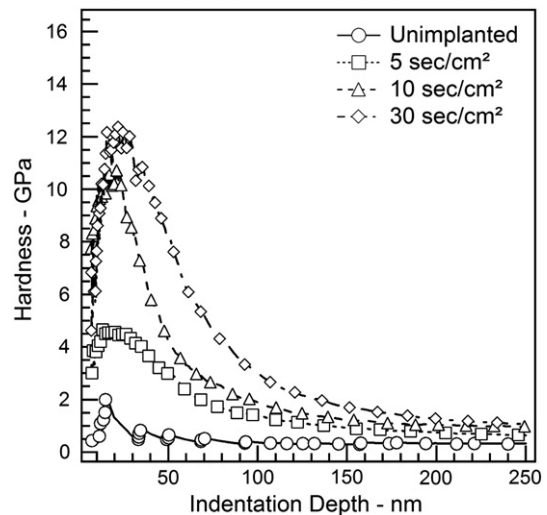| Implanted fluence (s/cm²)	Relative evolution of a_{Al}	AlN crystallite size (nm)
Unimplanted	–	0
10	+0.5%	4
20	+0.5%	4
30	−1.7%	5
40	−1.2%	7

Fig. 6. Typical hardness profiles of implanted Al-1050 samples.
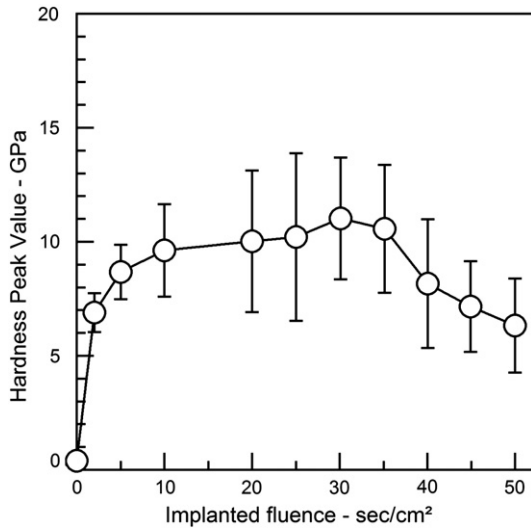
Fig. 7. Evolution of the average hardness peak value with the implanted fluence for Al-1050 alloy.

Table 4
Results of wear tests for unimplanted and implanted samples.

Implanted fluence (s/cm^2)	0	10	30	40	50	60
Number of laps before fracture	–	–	–	220	50	70
Wear rate after 40 laps (mm^3/Nm^{-1})	0.034	0.087	0.097	nwe[a]	0.021	0.035

[a] nwe = no wear evidence

protective nitride layer on aluminum alloys. Fig. 10 sums up the previous experimental results in a synthetic way. It illustrates the evolution of AlN crystallites size, Al-matrix lattice parameter a, hardness

Implanting 50 s/cm^2 and 60 s/cm^2 leads to the same tendency but with shorter layer longevity as we can see in Table 4. This table also indicates the wear rates measured after a tribological test stopped at 40 laps. The decrease of the friction coefficient observed for the 40 s/cm^2 implanted sample has the expected positive effect on surface wear. Moreover, wear is more intensive for insufficiently implanted samples (10 s/cm^2 and 30 s/cm^2) than for the pristine samples.

SEM observations of damaged and undamaged regions interface for unimplanted and 40 s/cm^2 implanted samples, after the layer fracture, are presented in Fig. 9(a)–(b). They clearly establish the apparition of cracks in the protective layer revealing the brittle behavior of the implanted surface. The virgin sample shows a very clean interface. After the fracture of the layer, abrasive particles appear, as evidenced in Fig. 9(c).

3.3. Origin of hardening and wear resistance enhancement of implanted Al-1050 alloy

The surface hardening and corresponding decrease of both friction coefficient and wear rate are strongly linked to the formation of a
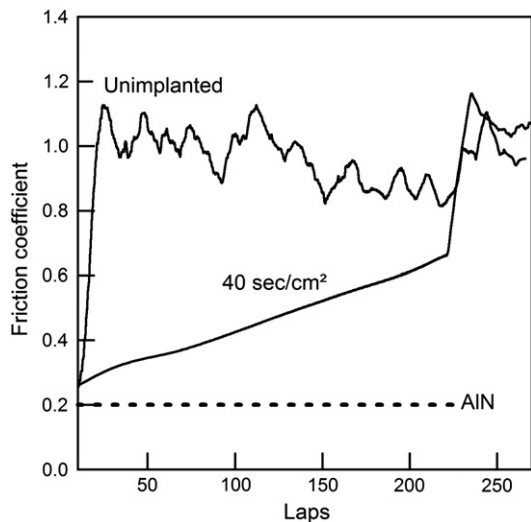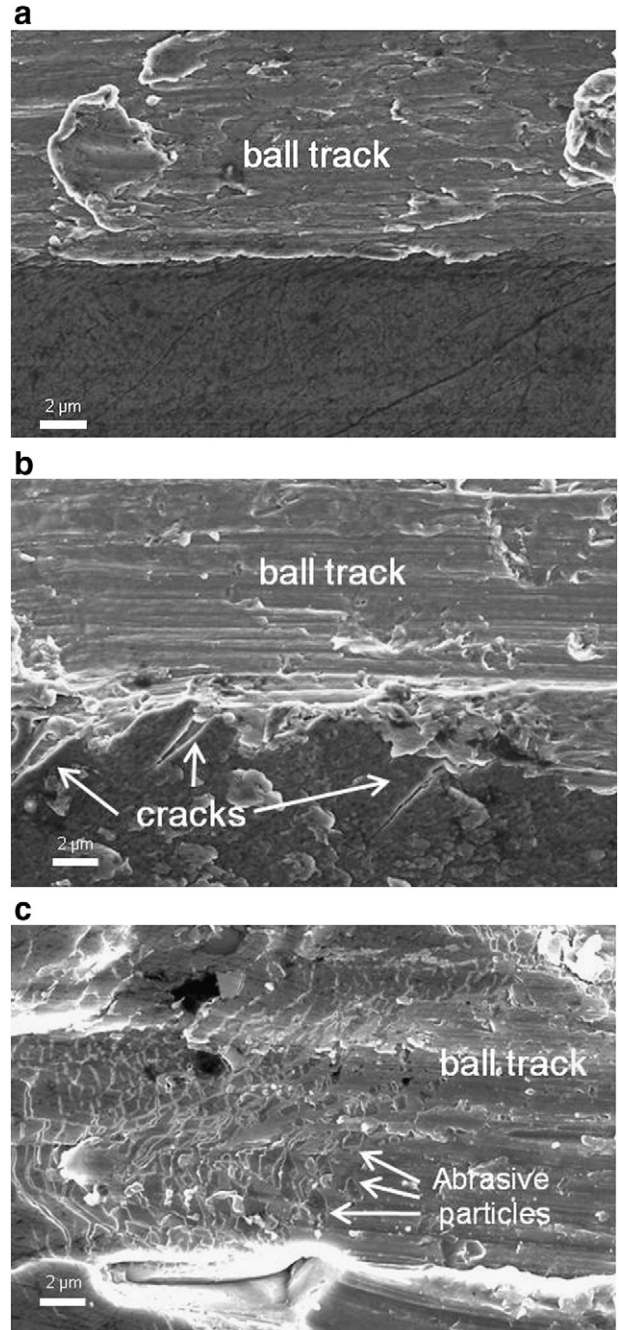

Fig. 8. Evolution of the friction coefficient for virgin and implanted Al-1050 samples. Pure AlN friction coefficient is given for comparison.

Fig. 9. SEM observation of the interface between damaged and undamaged zones after wear tests for (a) virgin and (b) 40 s/cm^2 implanted Al-1050 samples. (c) Presence of abrasive particles on the ball track of the 40 s/cm^2 implanted sample.
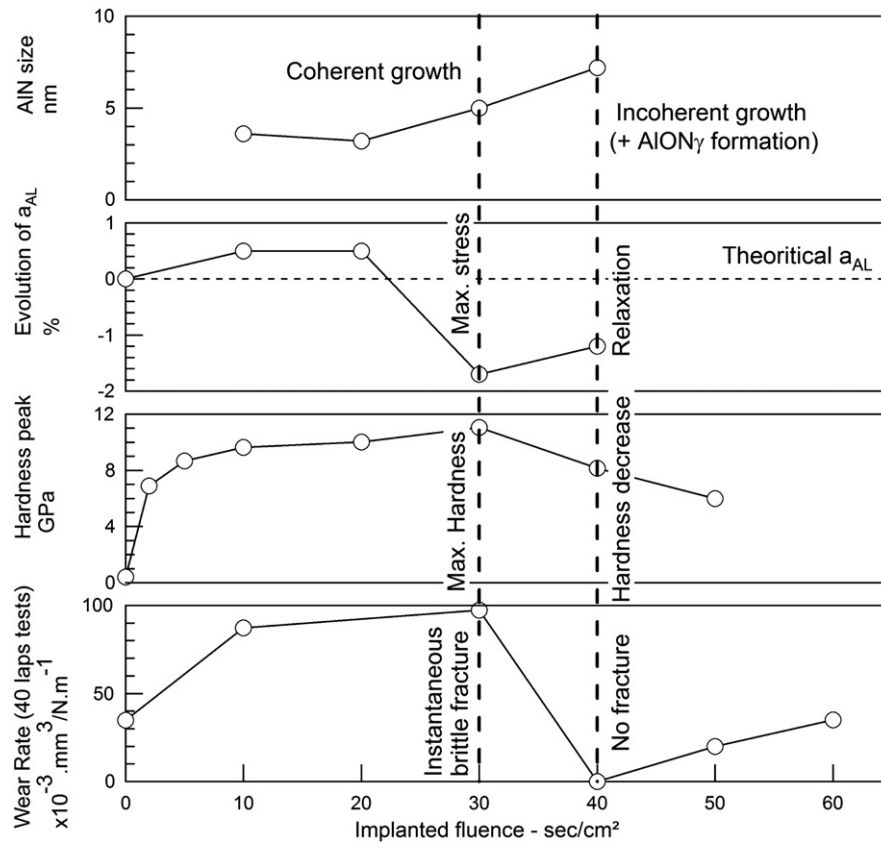
Fig. 10. Evolution of the AlN crystallite size, aluminum lattice parameter, maximum hardness and wear rate (after 40-lap tests) versus the implanted fluence for Al-1050.

profile peak and wear rate (40-lap tests) with the implanted fluence for Al-1050.

The strong hardening observed for weak fluence values confirms the solid solution hardening previously mentioned. The maximum hardness corresponds to the maximum strain of Al matrix due to coherent and generalized AlN precipitation in the implanted layer. At its maximum, hardness almost reaches the pure AlN hardness (12 GPa) which reveals the formation of a continuous nitride layer. A decrease in the hardness peak follows the second relaxation of Al-matrix probably due to incoherent AlN growth.

Regarding the tribological tests, one can observe that best results are not obtained with the same implantation conditions as the ones for hardness measurements. In fact, implantation must be operated for longer times to form an efficient protective layer. In the case of the 1050 alloy, XPS measurements have shown the presence of AlONγ in the extreme surface, which could be responsible for the observed wear resistance enhancement. Berriche et al. [40], have reported that AlONγ ceramics exhibit very low friction coefficients in the 0.2–0.5 range. It can also be observed that the effectiveness of protective layer occurs when the second relaxation begins, whereas maximum wear rate is obtained when the Al-matrix is strained at its highest value. After a 30 s/cm^2 N-implantation, internal stresses are reaching so high values that the contact between 100C6-ball and the stressed surface fractures the implanted layer and leads to the formation of abrasive particles rich in aluminum nitride, generating more severe wear regarding to the pristine sample. The best wear resistance behavior is therefore reached when a thin AlONγ layer covers a stabilized AlN layer.

When internal stresses start to decrease, aluminum presents a more stable and efficient protective surface. Despite the fact that a high hardness level is quickly obtained, implantation must be performed until the implanted layer reaches a stabilized state.

The brittle fracture observed for prolonged tests confirms the hypothesis that mainly the properties of AlN or AlONγ, ceramic compounds, are involved in the friction behavior of the implanted sample. Ceramic materials are known as brittle when submitted to wear tests [41]. The unimplanted sample shows only adhesive wear which is characteristic of pure (ductile) metal. One can also note that a decrease in roughness induced by surface sputtering is another factor involved in the wear rate decrease.

Similar tendencies are observed after implantation of Al-2024 alloys, with the only difference being that mechanical behavior changes occur at larger fluencies. Hardness quickly increases at low fluencies and reaches the maximum average hardness of 11 GPa after a 40 s/cm^2 implantation (Fig. 11(a)). The friction coefficient, initially around a value of 0.8, is not modified for implantation lower than 60 s/cm^2. For this critical fluence, corresponding to a hardness decrease, the friction coefficient drops down to a value of 0.2 and not sensitive wear is longer evidenced (Fig. 11(b)).

Implantation induced hardening seems therefore to be prominent among hardening mechanisms occurring in virgin alloys (strain hardening for Al-1050 and structural hardening for Al-2024). Thus, the maximum hardness of implanted samples does not depend on composition alloy or on initial hardening mechanism but is directly linked to nitride phase properties. In the case of aluminum hardening by N-implantation, the comparison of absolute hardness is more pertinent than using relative values as presented by several authors [38,42,43]. The same thing occurs regarding to wear resistance enhancement which is only due to the presence of a nitride protective layer and not to the initial surface properties. These facts signify that the presence of alloying elements only impedes the mechanisms responsible for surface reinforcement (higher fluences required) but does not change them. In other words, there is no new mechanism involved due to the implantation process but only the relative activities of the usual hard straining mechanisms are modified.
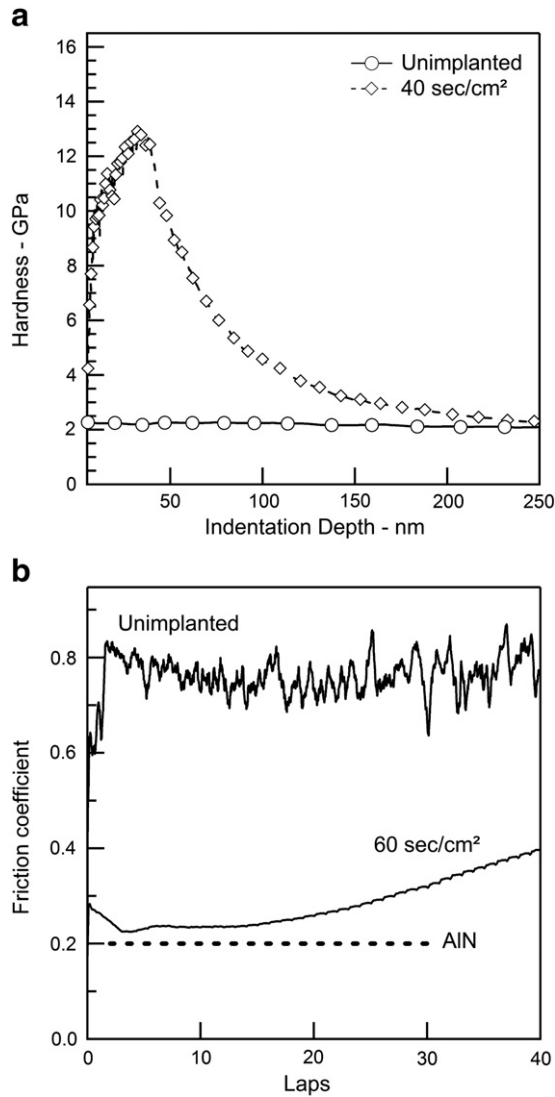
Fig. 11. (a) Hardness profiles of virgin and 40 s/cm² implanted Al-2024 samples. (b) Evolution of the friction coefficient for virgin and 60 s/cm² implanted Al-2024 samples. Pure AlN friction coefficient is given for comparison.

4. Conclusion

The present study, devoted to multicharged N-implantation effects upon superficial mechanical properties of aluminum alloys, leads to the following conclusions:

- Using a one-shot multi-charged implantation allows to obtain similar results in terms of hardness and wear resistance than those obtained with a three-steps and multi-energetic implantation.
- The low nitrogen concentration gradient revealed by XPS measurements leads to the formation of thin AlONγ, covering the AlN layer, at the origin of the hardening and the enhancement of wear resistance of aluminum.
- The original microstructure only affects the implantation fluence required to form the AlN layer but not the absolute hardness or wear behavior obtained after implantation. Structural-hardening (2024) and strain-hardening (1050) mechanisms become obsolete after implantation-hardening. Improvement in hardness and wear resistance are only due to the intrinsic properties of the ceramic protective layer (AlN and AlONγ).
- Internal stresses caused by microstructure evolution during implantation directly affect hardness and wear resistance. The relaxation

of the implanted layer needs to be reached to provide a good wear resistance and to avoid its premature brittle fracture and abrasive particles formation.

All of these results confirm the interest of using multi-charged ions implantation to enhance functional properties of aluminum alloys with a quicker and simpler way than mono-energetic implantation. This study also indicates that specific care must be taken to determine optimal implantation parameters leading to optimized microstructures, depending on the material composition.

References

[1] C. Blawert, B.L. Mordike, Nucl. Instrum. Methods Phys. Res. B 127–128 (1997) 873.
[2] J. Chakraborty, S. Mukherjee, P.M. Raole, P.I. John, Mater. Sci. Eng., A 304–306 (2001) 910.
[3] Y. Hara, T. Yamanishi, K. Azuma, H. Uchida, M. Yatsuzuka, Surf. Coat. Technol. 156 (2002) 166.
[4] S. Schoser, G. Brauchle, J. Forget, K. Kohlhof, T. Weber, J. Voigt, B. Rauschenbach, Surf. Coat. Technol. 103–104 (1998) 222.
[5] S. Lucas, J. Chevallier, Surf. Coat. Technol. 51 (1992) 441.
[6] S. Lucas, J. Chevallier, Surf. Coat. Technol. 65 (1994) 128.
[7] S. Lucas, J. Chevallier, N.G. Chechenin, Surf. Coat. Technol. 66 (1994) 334.
[8] S. Lucas, G. Terwagne, F. Bodart, Nucl. Instrum. Methods Phys. Res. B 50 (1990) 401.
[9] S. Lucas, G. Terwagne, M. Piette, F. Bodart, Nucl. Instrum. Methods Phys. Res. B 59–60 (1991) 925.
[10] B. Rauschenbach, K. Breuer, G. Leonhardt, Nucl. Instrum. Methods Phys. Res. B 47 (1990) 396.
[11] B. Rauschenbach, A. Kolitsch, E. Richter, Thin Solid Films 109 (1983) 37.
[12] L. Guzman, G. Bonini, M. Adami, P.M. Ossi, A. Miotello, M. Vittori-Antisari, A.M. Serventi, E. Voltolini, Surf. Coat. Technol. 83 (1996) 284.
[13] H.J. Kang, Int. J. Precis. Eng. Manuf. 7 (2006) 57.
[14] J.P. Riviere, P. Meheust, J.P. Villain, Surf. Coat. Technol. 158–159 (2002) 647.
[15] L. Martinez Orellana, F.J. Perez, C. Gomez, Surf. Coat. Technol. 200 (2005) 1609.
[16] F. Guernalec, D. Busardo, (2005) France, patent number: WO2005085491.
[17] R. Geller, Electron Cyclotron Resonance Ion Sources and Ecran Plasmas, I.O.P. Publishing, 1996.
[18] S. Thibault, Ph D Thesis, Université de Caen Basse-Normandie, 2009.
[19] Y. Miyagawa, S. Nakao, M. Ikeyama, K. Saitoh, S. Miyagawa, Nucl. Instrum. Methods Phys. Res. B 127–128 (1997) 765.
[20] L. Lutterotti, S. Matthies, H.-R. Wenk, in: J.A. Szpunar (Ed.), Textures of Materials, NRC Research Press, Ottawa, 1999, p. 1599.
[21] H.-M. Rietveld, Acta Crystallogr. 22 (1967) 151.
[22] L. Lutterotti, Nucl. Instrum. Methods Phys. Res. B 268 (2010) 334.
[23] D. Chateigner, Combined Analysis, ISTE Ltd and John Wiley & Sons Inc., 2010
[24] S. Grazulis, D. Chateigner, R.T. Downs, A.T. Yokochi, M. Quiros, L. Lutterotti, E. Manakova, J. Butkus, P. Moeck, A.L. Bail, J. Appl. Crystallogr. 42 (2009) 726.
[25] E. Leblond, Ph D Thesis, Ecole Centrale de Lyon, 1998.
[26] S. Ohira, M. Iwaki, Nucl. Instrum. Methods Phys. Res. B 19–20 (1987) 162.
[27] W. Österle, I. Dörfel, I. Urban, T. Reier, J.W. Schultze, Surf. Coat. Technol. 102 (1998) 168.
[28] T. Reier, J.W. Schultze, W. Österle, C. Buchal, Thin Solid Films 385 (2001) 29.
[29] C.A. Figueroa, F. Alvarez, Appl. Surf. Sci. 253 (2006) 1806.
[30] J.W. McCauley, P. Patel, M. Chen, G. Gilde, E. Strassburger, B. Paliwal, K.T. Ramesh, D.P. Dandekar, J. Eur. Ceram. Soc. 29 (2009) 223.
[31] R.W.G. Wyckoff, Crystal Structures, 2nd ed. Interscience Publishers, New York, 1963.
[32] J. Mendez, P. Violan, M.F. Denanot, Nucl. Instrum. Methods Phys. Res. B 19–20 (1987) 232.
[33] K.C. Walter, R.A. Dodd, J.R. Conrad, Nucl. Instrum. Methods Phys. Res. B 106 (1995) 522.
[34] D. Rémiens, L. Yang, F. Ponchel, J.F. Légier, D. Chateigner, G. Wang, J. Appl. Phys. 109 (2011) 114106.
[35] H.L. Lu, W.F. Sommer, M.J. Borden, J.R. Tesmer, X.D. Wu, Thin Solid Films 289 (1996) 17.
[36] A.P. Matthews, M. Iwaki, Y. Horino, M. Satou, K. Yabe, Nucl. Instrum. Methods Phys. Res. B 59–60 (1991) 671.
[37] S. Seghrouchni, Thesis, Université de Strasbourg (1996).
[38] T.R. Jervis, H.-L. Lu, J.R. Tesmer, Nucl. Instrum. Methods Phys. Res. B 72 (1992) 59.
[39] R.J. Rodriguez, A. Sanz, A. Medrano, J. Garcia-Lorente, Vacuum 52 (1999) 187.
[40] Y. Berriche, J. Vallayer, R. Trabelsi, D. Treheux, J. Eur. Ceram. Soc. 20 (2000) 1311.
[41] K.-H. Zum Gahr, Microstructure and Wear of Materials, Elsevier Science Publishers B.V., New York, 1987.
[42] P. Budzynski, A.A. Youssef, Z. Surowiec, R. Paluch, Vacuum 81 (2007) 1154.
[43] I. Madakson, J. Phys. D 18 (1985) 531.